INTERNATIONAL JOURNAL FOR NUMERICAL METHODS IN FLUIDS
Int. J. Numer. Meth. Fluids 2006; **52**:659–678
Published online 17 February 2006 in Wiley InterScience (www.interscience.wiley.com). DOI: 10.1002/fld.1194

Scaled boundary finite element analysis of the water sloshing in 2D containers

B. Teng[1,*,†], M. Zhao[2,‡] and G. H. He[1,§]

[1]*State Key Laboratory of Coastal and Offshore Engineering, Dalian University of Technology, Dalian 116024, China*
[2]*School of Civil and Resource Engineering, The University of Western Australia, 35 Stirling Highway, Crawley, WA 6009, Australia*

SUMMARY

In this paper, the water sloshing in a 2D container is simulated numerically. The 2D Laplace equation is solved by using the scaled boundary finite element method (SBFEM) based on the linearized free surface boundary condition. The computational results are compared with the analytical solution and solutions from a finite element method (FEM). It is found that the SBFEM method gives much better results than the FEM method in the case of same mesh size. The effect of the oscillating frequency on the amplitude of the surface elevation is also investigated. Copyright © 2006 John Wiley & Sons, Ltd.

KEY WORDS: SBFEM; slosh; water waves

1. INTRODUCTION

The scaled boundary finite element method (SBFEM) is a numerical method for solving the linear differential equations semi-analytically. By using this method, only the boundary of the computational domain is discretized. SBFEM reduces the dimension of the computational domain by one comparing with the finite element method (FEM). An analytical method is applied in the reduced direction. The SBFEM can be applied to hyperbolic, parabolic and elliptic problems [1–3]. It did not need the fundamental solution comparing with the boundary

*Correspondence to: B. Teng, State Key Laboratory of Coastal and Offshore Engineering, Dalian University of Technology, Dalian 116024, China.
†E-mail: bteng@dlut.edu.cn
‡E-mail: zhao@civil.uwa.edu.au
§E-mail: heguhu@163.com

Contract/grant sponsor: National Natural Science Foundation of China; contract/grant number: 10372020
Contract/grant sponsor: Program for Changjiang Scholars and Innovative Research Team in University; contract/grant number: IRTO420

Received 29 July 2005
Revised 2 January 2006
Accepted 7 January 2006

Copyright © 2006 John Wiley & Sons, Ltd.

element method (BEM) and the singularity of the integration, which is encountered in BEM can also be avoided in SBFEM.

Recently, Deeks and Cheng [4] established a SBFEM method for simulating the potential flow past obstacles. The results of their work proved the advantage of the SBFEM method over the conventional finite difference method (FDM). Li *et al.* [5] developed a scaled boundary finite element solution of Helmholtz equation for wave diffraction by a vertical cylinder.

In this study, a SBFEM model is developed for simulating the water sloshing in a 2D container. The Laplace equation is solved in the scaled coordinate system. The scaled centre is located at a point on the still water surface. The SBFEM formulation is established and solved. An eigenvalue problem of a Hamiltonian matrix is solved. Because the present Hamiltonian matrix contains two zero eigenvalues corresponding to two dependent eigenvectors, the Jordan decomposition is applied to it. The model is applied to simulate the water sloshing in a rectangular tank and that in a hemi-circular tank. The computational results are compared with the analytical solution and those from a FEM. The numerical results show that the predicted velocity in the direction of the scaled coordinate is much more accurate than those from FEM because the analytical method is employed in this direction. The effects of the water depth in the water container and the oscillating frequency on the amplitude of the surface fluctuation are also investigated.

2. GOVERNING EQUATIONS AND BOUNDARY CONDITIONS

Water sloshing in a 2D container is considered. The fluid is assumed to be inviscid and incompressible. The motion of the fluid in the container is assumed to be irrotational. There exists a scalar potential function Φ, which satisfies the following Laplace equation:

$$\nabla^2 \Phi = 0 \tag{1}$$

within the computational domain Ω.

Assuming the motion of the wave surface is simple harmonic in time with an angular frequency ω, we can separate out the time factor and write the velocity potential as follows:

$$\Phi(x,z,t) = \mathrm{Re}[\phi(x,z)\mathrm{e}^{-\mathrm{i}\omega t}] \tag{2}$$

The complex potential ϕ in Equation (2) also satisfies the Laplace equation (Equation (1)). In the case of the water sloshing in a 2D container (as shown in Figure 1), the linearized boundary conditions for velocity potential are as follows:

(1) The free surface condition

$$\frac{\partial \phi}{\partial z} = k_0 \phi \tag{3}$$

where $k_0 = \omega^2/g$ and g is the gravitational acceleration.

(2) At the body surface, the normal velocity of the fluid is the same as that of the container wall

$$\frac{\partial \phi}{\partial n} = v_n^{\mathrm{b}} \tag{4}$$

Copyright © 2006 John Wiley & Sons, Ltd.

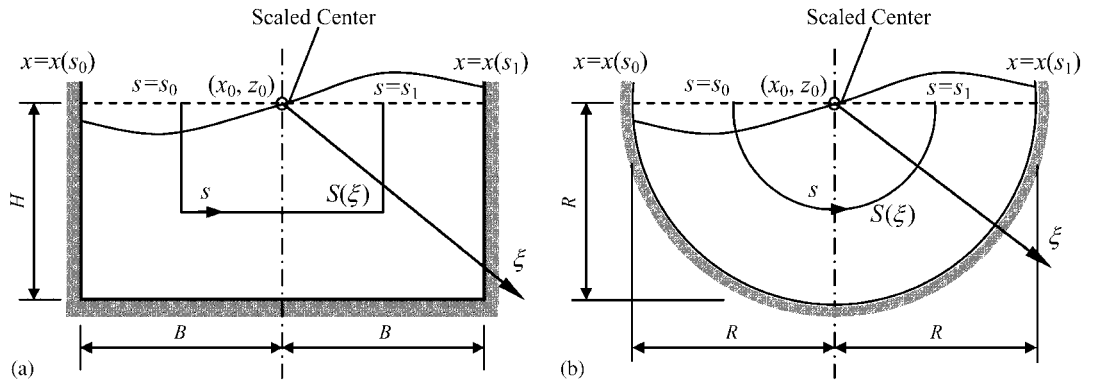

Figure 1. The definition of the scaled coordinate: (a) rectangular tank; and (b) hemi-circular tank.

where v_n^b is the velocity component of the container wall in the normal direction of the boundary.

The fluid velocity is related to the potential function as

$$\{u\} = \nabla\phi \tag{5}$$

3. FORMULATION OF THE SCALED BOUNDARY FINITE ELEMENT METHOD

Figures 1(a) and (b) are definition of the scaled coordinate system for two examples of a rectangular water tank and a hemi-circular one, respectively. As shown in Figure 1, we choose a point (x_0, z_0) on the still surface as the scaled centre. The computational domain is in the region $(0 \leqslant \xi \leqslant 1)$ with $\xi = 0$ at the scaled centre and $\xi = 1$ on the boundary. The mapping between the scaled coordinate system and the Cartesian coordinate system can be expressed by the scaling equations

$$x(\xi, s) = x_0 + \xi\hat{x}(s) \tag{6a}$$

$$z(\xi, s) = z_0 + \xi\hat{z}(s) \tag{6b}$$

where $\hat{x}(s) = x(s) - x_0$, $\hat{z}(s) = z(s) - z_0$ are the local coordinates of the container's boundary relative to the scaled centre. The coordinate of a point in the domain can be uniquely represented by the scaled coordinate ξ and the local coordinate s along the curve $S(\xi)$. To transform the gradient operator ∇ in the xy coordinate system to that in the ξs coordinate system, the Jacobian matrix is required

$$[\hat{J}(\xi, s)] = \begin{bmatrix} x_{,\xi} & z_{,\xi} \\ x_{,s} & z_{,s} \end{bmatrix} = \begin{bmatrix} 1 & 0 \\ 0 & \xi \end{bmatrix} [J(s)] \tag{7}$$

Copyright © 2006 John Wiley & Sons, Ltd.

where the abbreviation $[J(s)]$ is defined by

$$[J(s)] = \begin{bmatrix} \hat{x} & \hat{z} \\ \hat{x}_{,s} & \hat{z}_{,s} \end{bmatrix} \tag{8}$$

Using Equations (7) and (8), the infinitesimal area $\mathrm{d}\Omega$ can be expressed by ξ and s as

$$\mathrm{d}\Omega = \xi |J| \, \mathrm{d}\xi \, \mathrm{d}s \tag{9}$$

Applying the weighted residual method to the Laplace equation, we can obtain the following integral equation:

$$\int_{\Omega} \nabla W(\xi, s) \cdot \nabla \phi(\xi, s) \, \mathrm{d}\Omega - \int_{\Gamma} W(\xi, s) v_n \, \mathrm{d}\Gamma = 0 \tag{10}$$

where $W(x, s)$ is the weighting function, Γ represents the boundary of the computational domain, v_n is the velocity component in the normal direction of the boundary pointing out of the fluid. The curve $S(\xi)$ is discretized into several second-order three-node piecewise finite elements. The potential along $S(\xi)$ can be approximately expressed by

$$\phi(\xi, s) = \{N(s)\}^{\mathrm{T}} \{a(\xi)\} \tag{11}$$

where $a(\xi)$ is the nodal values of the potential function, $\{N(s)\}$ is the shape function vector. In the scaled coordinate system, the gradient operator ∇ can be expressed as

$$\nabla = \{b^1(s)\} \frac{\partial}{\partial \xi} + \frac{1}{\xi} \{b^2(s)\} \frac{\partial}{\partial s} \tag{12}$$

where $\{b^1(s)\}$ and $\{b^2(s)\}$ are defined as

$$\{b^1(s)\} = \frac{1}{|J|} \begin{Bmatrix} z(s)_{,s} \\ -x(s)_{,s} \end{Bmatrix}, \quad \{b^2(s)\} = \frac{1}{|J|} \begin{Bmatrix} -z(s) \\ x(s) \end{Bmatrix} \tag{13}$$

where $|J| = x(s) z(s)_{,s} - x(s)_{,s} \, z(s)$, and the subscript represents the partial differential with the corresponding variable. Utilizing Equations (11) and (12), the gradient operator can be expressed as

$$\nabla = [B^1(s)] \frac{\partial}{\partial \xi} + \frac{1}{\xi} [B^2(s)] \frac{\partial}{\partial s} \tag{14}$$

where the matrices $[B^1(s)]$ and $[B^2(s)]$ are defined as

$$[B^1(s)] = \{b^1(s)\} \{N(s)\}^{\mathrm{T}}, \quad [B^2(s)] = \{b^2(s)\} \{N(s)\}^{\mathrm{T}}_{,s} \tag{15}$$

The weighting function $W(\xi, s)$ is also interpolated by its nodal values and the shape functions as

$$W(\xi, s) = \{N(s)\}^{\mathrm{T}} \{w(\xi)\} \tag{16}$$

Copyright © 2006 John Wiley & Sons, Ltd.

Substituting Equations (14) and (16) in Equation (10) for arbitrary $\{w(\xi)\}$, the integration over the domain Ω in Equation (10) with respect to ξ from ξ_0 to ξ_1 can be expressed as

$$\begin{aligned} \mathrm{I}_\Omega &= \int_\Omega \nabla W(\xi,s)\cdot\nabla\phi(\xi,s)\,\mathrm{d}\Omega \\ &= \int_{\xi_0}^{\xi_1} \Big(\xi\{w(\xi)\}^{\mathrm{T}}_{,\xi}([E^0]\{a(\xi)\}_{,\xi}+[E^1]^{\mathrm{T}}\{a(\xi)\}) \\ &\quad + \{w(\xi)\}^{\mathrm{T}}\Big([E^1]\{a(\xi)\}_{,\xi}+\frac{1}{\xi}[E^2]\{a(\xi)\}\Big)\Big)\,\mathrm{d}\xi \end{aligned} \tag{17}$$

where the matrices in Equation (17) are defined as

$$[E^0] = \int_{S(\xi)} [B^1(s)]^{\mathrm{T}}[B^1(s)]|J|\,\mathrm{d}s \tag{18a}$$

$$[E^1] = \int_{S(\xi)} [B^2(s)]^{\mathrm{T}}[B^1(s)]|J|\,\mathrm{d}s \tag{18b}$$

$$[E^2] = \int_{S(\xi)} [B^2(s)]^{\mathrm{T}}[B^2(s)]|J|\,\mathrm{d}s \tag{18c}$$

Integrating terms containing $w(\xi)_{,\xi}$ in Equation (17) yields

$$\begin{aligned} \mathrm{I}_\Omega = &\int_{\xi_0}^{\xi_1} \{w(\xi)\}^{\mathrm{T}}\left(-\xi[E^0]\{a(\xi)\}_{,\xi\xi} + ([E^1]-[E^0]-[E^1]^{\mathrm{T}})\{a(\xi)\}_{,\xi} + \frac{1}{\xi}[E^2]\{a(\xi)\}\right)\mathrm{d}\xi \\ &+ \{w(\xi_1)\}^{\mathrm{T}}(\xi_1[E^0]\{a(\xi_1)\}_{,\xi} + [E^1]^{\mathrm{T}}\{a(\xi_1)\}) - \{w(\xi_0)\}^{\mathrm{T}}(\xi_0[E^0]\{a(\xi_0)\}_{,\xi} \\ &+ [E^1]^{\mathrm{T}}\{a(\xi_0)\}) \end{aligned} \tag{19}$$

Along the free surface boundaries $s=s_0$ and $s=s_1$ the infinitesimal integrating length can be expressed as $\mathrm{d}\Gamma = |x(s_0)-x_0|\,\mathrm{d}\xi$ and $\mathrm{d}\Gamma = |x(s_1)-x_0|\,\mathrm{d}\xi$, respectively. Utilizing the free surface boundary condition (Equation (4)), the integration over the boundary of the domain in Equation (10) with ξ from ξ_0 to ξ_1 can be expressed as

$$\mathrm{I}_\Gamma = -\int_\Gamma \{w(\xi)\}^{\mathrm{T}}\{N(s)\}v_n\,\mathrm{d}\Gamma = \int_{\xi_0}^{\xi_1} \{w(\xi)\}^{\mathrm{T}}[G]\{a(\xi)\}\,\mathrm{d}\xi - \{q(\xi_0)\} - \{q(\xi_1)\} \tag{20}$$

where

$$[G] = -k_0(\{N(s_0)\}\{N(s_0)\}^{\mathrm{T}}|x(s_0)-x_0| + \{N(s_1)\}\{N(s_1)\}^{\mathrm{T}}|x(s_1)-x_0|) \tag{21}$$

$$\{q(\xi)\} = \int_{S(\xi)} \{w(\xi)\}^{\mathrm{T}}\{N(s)\}v_n\,\mathrm{d}\Gamma \tag{22}$$

Copyright © 2006 John Wiley & Sons, Ltd.

Finally, the integration equation (10) can be written as

$$
\begin{aligned}
&-\int_{\xi_0}^{\xi_1}\{w(\xi)\}^{\mathrm{T}}\frac{1}{\xi}(\xi^2[E^0]\{a(\xi)\}_{,\xi\xi}\\
&\quad+\xi([E^0]-[E^1]+[E^1]^{\mathrm{T}})\{a(\xi)\}_{,\xi}-([E^2]+\xi[G])\{a(\xi)\})\,\mathrm{d}\xi\\
&\quad+\{w(\xi_1)\}^{\mathrm{T}}([E^0]\xi_1[a(\xi_1)]_{,\xi}+[E^1]^{\mathrm{T}}[a(\xi_1)]-q\{\xi_1\})\\
&\quad-\{w(\xi_0)\}^{\mathrm{T}}([E^0]\xi_0[a(\xi_0)]_{,\xi}+[E^1]^{\mathrm{T}}[a(\xi_0)]-q\{\xi_0\})
\end{aligned}
\tag{23}
$$

Since Equation (23) should be satisfied for any set of weighting function $\{w(\xi)\}$ and any value of ξ_0 and ξ_1, the following conditions must be met:

$$\xi^2[E^0]\{a(\xi)\}_{,\xi\xi}+\xi([E^0]-[E^1]+[E^1]^{\mathrm{T}})\{a(\xi)\}_{,\xi}-([E^2]+\xi[G])\{a(\xi)\}=0 \tag{24}$$

$$q\{\xi\}=[E^0]\xi[a(\xi)]_{,\xi}+[E^1]^{\mathrm{T}}[a(\xi)] \tag{25}$$

The present *scaled boundary finite element* equations (Equations (24) and (25)) are similar to those by Song and Wolf [6]. The only difference is the last term of Equation (24).

4. SOLUTION OF THE SCALED BOUNDARY FINITE ELEMENT EQUATIONS

By making a transformation

$$\xi=\frac{\bar{\xi}^2}{2} \tag{26}$$

the derivative with respect to ξ can be transformed as

$$\frac{\partial}{\partial\xi}=\frac{1}{\bar{\xi}}\frac{\partial}{\partial\bar{\xi}} \tag{27a}$$

$$\frac{\partial^2}{\partial\xi^2}=\frac{1}{\bar{\xi}^2}\frac{\partial}{\partial\bar{\xi}^2}-\frac{1}{\bar{\xi}^3}\frac{\partial}{\partial\bar{\xi}} \tag{27b}$$

Using Equation (27), Equations (24) and (25) can be written as

$$[E^0]\frac{\bar{\xi}^2}{2}\{a(\bar{\xi})\}_{,\bar{\xi}\bar{\xi}}+\left(\frac{[E^0]}{2}-[E^1]+[E^1]^{\mathrm{T}}\right)\bar{\xi}\{a(\bar{\xi})\}_{,\bar{\xi}}-(2[E^2]+\bar{\xi}^2[G])\{a(\bar{\xi})\}=0 \tag{28}$$

$$\{q(\bar{\xi})\}=[E^0]\frac{\bar{\xi}}{2}\{a(\bar{\xi})\}_{,\bar{\xi}}+[E^1]^{\mathrm{T}}\{a(\bar{\xi})\} \tag{29}$$

From Equation (29), we can obtain

$$\bar{\xi}\{a(\bar{\xi})\}_{,\bar{\xi}}=-2[E^0]^{-1}[E^1]^{\mathrm{T}}\{a(\bar{\xi})\}+2[E^0]^{-1}\{q(\bar{\xi})\} \tag{30}$$

Copyright © 2006 John Wiley & Sons, Ltd.

Derivative of Equation (29) with respect to $\bar{\xi}$ is

$$\{q(\bar{\xi})\}_{,\bar{\xi}} = [E^0]\frac{\bar{\xi}}{2}\{a(\bar{\xi})\}_{,\bar{\xi}\bar{\xi}} + \left(\frac{[E^0]}{2} + [E^1]^{\mathrm{T}}\right)\{a(\bar{\xi})\}_{,\bar{\xi}} \tag{31}$$

Substituting Equation (28) in Equation (31), it yields

$$\bar{\xi}\{q(\bar{\xi})\}_{,\bar{\xi}} = (-2[E^1][E^0]^{-1}[E^1]^{\mathrm{T}} + 2[E^2])\{a(\bar{\xi})\} + 2[E^1][E^0]^{-1}\{q(\bar{\xi})\} + \bar{\xi}^2[G]\{a(\bar{\xi})\} = 0 \tag{32}$$

We write Equations (30) and (32) in the following form:

$$\bar{\xi}\{X(\bar{\xi})\}_{,\bar{\xi}} = -[Z]\{X(\bar{\xi})\} - \bar{\xi}^2\begin{bmatrix} 0 & 0 \\ -G & 0 \end{bmatrix}\{X(\bar{\xi})\} \tag{33}$$

with the definition of

$$\{X(\bar{\xi})\} = \begin{Bmatrix} \{a(\bar{\xi})\} \\ \{q(\bar{\xi})\} \end{Bmatrix}, \quad [Z] = \begin{bmatrix} 2[E^0]^{-1}[E^1]^{\mathrm{T}} & -2[E^0]^{-1} \\ 2[E^1][E^0]^{-1}[E^1]^{\mathrm{T}} - 2[E^2] & -2[E^1][E^0]^{-1} \end{bmatrix} \tag{34}$$

There is an independent set of solutions grouped in the matrix $[X(\bar{\xi})]$ of Equation (34). The general solution $\{X(\bar{\xi})\}$ can be expressed as

$$\{X(\bar{\xi})\} = [X(\bar{\xi})]\{c\} \tag{35}$$

with $\{c\}$ being the constant vector and $[X(\bar{\xi})]$ satisfies Equation (33)

$$\bar{\xi}[X(\bar{\xi})]_{,\bar{\xi}} = -[Z][X(\bar{\xi})] - \bar{\xi}^2\begin{bmatrix} 0 & 0 \\ -[G] & 0 \end{bmatrix}[X(\bar{\xi})] \tag{36}$$

The eigendecomposition of the Hamiltonian matrix $[Z]$ is as

$$[Z][V] = -[V][\Lambda] \tag{37}$$

where $[V]$ is the matrix of the eigenvectors, and the eigenvalues of $[Z]$ consist of two groups with opposite signs

$$[\Lambda] = \begin{bmatrix} -[\lambda_j] & \\ & [\lambda_j] \end{bmatrix} \tag{38}$$

where $\mathrm{Re}(\lambda_j) \leqslant 0$.

There is a pair of zero eigenvalues in Equation (38). The mode corresponding to zero eigenvalue represents the constant potential in the entire fluid domain. The eigenvectors of the two zero eigenvalues are not independent, leading to a singular matrix $[V]$. The irreversibility of $[V]$ make $[Z]$ cannot be transformed to a diagonal matrix. In this study, the Jordan decomposition is applied to the matrix [Z]

$$[Z][\Psi] = -[\Psi][\bar{\Lambda}] \tag{39}$$

Copyright © 2006 John Wiley & Sons, Ltd.

where the Jordan matrix

$$[\bar{\Lambda}] = \begin{bmatrix} -[\lambda_j] & & & \\ & 0 & -1 & \\ & & 0 & \\ & & & [\lambda_j] \end{bmatrix} \tag{40}$$

Introducing the matrix $[W(\bar{\xi})]$ defined as

$$[X(\bar{\xi})] = [\Psi][W(\bar{\xi})] \tag{41}$$

Equation (36) can be written as

$$\bar{\xi}[W(\bar{\xi})]_{,\bar{\xi}} = [\bar{\Lambda}][W(\bar{\xi})] - \bar{\xi}^2[M][W(\bar{\xi})] \tag{42}$$

where

$$[M] = [\Psi]^{-1} \begin{bmatrix} 0 & 0 \\ -[G] & 0 \end{bmatrix} [\Psi] \tag{43}$$

The solution of Equation (42) is written as the product of two square matrix functions in $\bar{\xi}$

$$[W(\bar{\xi})] = [A(\bar{\xi})][Y(\bar{\xi})] \tag{44}$$

The first matrix $[A(\bar{\xi})]$ is formulated as a power series in $\bar{\xi}$ as

$$[A(\bar{\xi})] = [A_0] + \bar{\xi}^2[A_1] + \bar{\xi}^4[A_2] + \cdots + \bar{\xi}^{2k}[A_k] + \cdots \tag{45}$$

with $[A_0] = [I]$, and the other coefficient matrices $[A_k]$ to be determined. The matrix $[Y(\bar{\xi})]$ in Equation (44) satisfies the following ordinary differential equations:

$$\bar{\xi}[Y(\bar{\xi})]_{,\bar{\xi}} = [P^*(\bar{\xi})][Y(\bar{\xi})] \tag{46}$$

where $[P^*(\bar{\xi})]$ is also a power series in $\bar{\xi}$

$$[P^*(\bar{\xi})] = [P_0^*] + \bar{\xi}^2[P_1^*] + \bar{\xi}^4[P_2^*] + \cdots + \bar{\xi}^{2k}[P_k^*] + \cdots \tag{47}$$

with $[P_0^*] = [\Lambda]$. Utilizing Equations (44) and (46), the derivation of $[W(\bar{\xi})]$ can be expressed as

$$[W(\bar{\xi})]_{,\bar{\xi}} = ([A(\bar{\xi})]_{,\bar{\xi}} + \frac{1}{\bar{\xi}}[A(\bar{\xi})][P^*(\bar{\xi})])[Y(\bar{\xi})] \tag{48}$$

Substituting Equations (44) and (48) in Equation (42) results in

$$\bar{\xi}[A(\bar{\xi})]_{,\bar{\xi}} - [\bar{\Lambda}][A(\bar{\xi})] + [A(\bar{\xi})][P^*(\bar{\xi})] + \bar{\xi}^2[M][A(\bar{\xi})] = 0 \tag{49}$$

Copyright © 2006 John Wiley & Sons, Ltd.

Substituting Equations (45) and (47) in Equation (49) leads to a power series of $\bar{\xi}$

$$[P_0^*] - [\bar{\Lambda}] + \bar{\xi}^2(-[\bar{\Lambda}][A_1] + [A_1][\bar{\Lambda}] + 2[A_1] + [P_1^*] + [M]) + \cdots + \bar{\xi}^{2k}(-[\bar{\Lambda}][A_k] + [A_k][\bar{\Lambda}] + 2k[A_k] + [P_k^*] + [C_k]) + \cdots = 0 \tag{50}$$

where $[C_k] = [M][A_{k-1}] + \sum_{i=1}^{k-1}[A_i][P_{k-i}^*]$. To satisfy Equation (50), the coefficients of the power series in $\bar{\xi}$ must vanish. This yields

$$[P_0^*] = [\bar{\Lambda}] \tag{51}$$

$$[\bar{\Lambda}][A_k] - [A_k][\bar{\Lambda}] - 2k[A_k] = [P_k^*] + [C_k] \quad k = 1, 2, \ldots \tag{52}$$

Equation (52) can be written as the following scalar equations:

$$\alpha_{ij}[A_k]_{ij} = [P_k^*]_{ij} + [C_k]_{ij} + \beta_{ij} \tag{53}$$

where the coefficients α_{ij} and β_{ij} are as

$$\alpha_{ij} = \begin{cases} \Lambda_i - \Lambda_j - 2k, & i \neq n, n+1 \text{ and } j \neq n, n+1 \\ \Lambda_i - 2k, & i \neq n, n+1 \text{ and } j = n, n+1 \\ -\Lambda_j - 2k, & i = n, n+1 \text{ and } j \neq n, n+1 \\ -2k, & i = n, n+1 \text{ and } j = n, n+1 \end{cases}$$

$$\beta_{ij} = \begin{cases} -[A_k]_{i,j-1}, & i \neq n \text{ and } j = n+1 \\ [A_k]_{i+1,j}, & i = n \text{ and } j \neq n+1 \\ -[A_k]_{i+1,j} - [A_k]_{i,j-1}, & i = n \text{ and } j = n+1 \\ 0 & \text{otherwise} \end{cases}$$

where $\Lambda_j = -\lambda_j$ and n is the nodal point number of the computational mesh. The similar approach by Song and Wolf [7] is applied to determine the matrices $[P_k^*]$ and $[A_k]$.

$$[P_k^*]_{ij} = \begin{cases} 0, & \alpha_{ij} \neq 0 \\ -[C_k]_{ij} - \beta_{ij}, & \alpha_{ij} = 0 \end{cases} \tag{54}$$

$$[A_k]_{ij} = \begin{cases} \dfrac{[C_k]_{ij} - \beta_{ij}}{\alpha_{ij}}, & \alpha_{ij} \neq 0 \\ \text{arbitrary}, & \alpha_{ij} = 0 \end{cases} \tag{55}$$

The matrix $[P^*(\bar{\xi})]$ is reformulated as

$$[P^*(\bar{\xi})] = [\Lambda] + \bar{\xi}^{[\Lambda]}[U]\bar{\xi}^{-[\Lambda]} \tag{56}$$

Copyright © 2006 John Wiley & Sons, Ltd.

with $[U]$ being a upper-triangular matrix with zeros on the diagonal

$$[U]=\begin{bmatrix} 0 & [\mathrm{P}^*]_{12} & [\mathrm{P}^*]_{13} & \cdots & [\mathrm{P}^*]_{1\mathrm{N}} \\ & 0 & [\mathrm{P}^*]_{23} & \ldots & [\mathrm{P}^*]_{2\mathrm{N}} \\ & & 0 & \cdots & [\mathrm{P}^*]_{3\mathrm{N}} \\ & & & \ddots & \vdots \\ & & & & 0 \end{bmatrix} \tag{57}$$

Substituting (56) in Equation (46) yields the ordinary differential equation for $[Y(\bar{\xi})]$

$$\bar{\xi}[Y(\bar{\xi})]_{,\bar{\xi}}=([\Lambda]+\bar{\xi}^{[\Lambda]}[U]\bar{\xi}^{-[\Lambda]})[Y(\bar{\xi})] \tag{58}$$

By introducing a square matrix $[\bar{Y}(\bar{\xi})]$ which is related to the $[Y(\bar{\xi})]$ as

$$[Y(\bar{\xi})]=\bar{\xi}^{-[\Lambda]}[\bar{Y}(\bar{\xi})] \tag{59}$$

we can get the following Euler–Cauchy equation:

$$\bar{\xi}[\bar{Y}(\bar{\xi})]_{,\bar{\xi}}=[U][\bar{Y}(\bar{\xi})] \tag{60}$$

The solution of Equation (60) is

$$[\bar{Y}(\bar{\xi})]=\bar{\xi}^{[U]}=\mathrm{e}^{[U]\ln\bar{\xi}}=[I]+[U]\ln\bar{\xi}+\frac{1}{2!}[U]^2(\ln\bar{\xi})^2+\cdots+\frac{1}{m!}[U]^m(\ln\bar{\xi})^m \quad m<N \tag{61}$$

Substituting Equation (61) backwards in Equations (59), (44) and (41) results in the analytical solution of Equation (36)

$$[X(\bar{\xi})]=[\Psi][A(\bar{\xi})]\bar{\xi}^{[\Lambda]}\bar{\xi}^{[U]} \tag{62}$$

Substituting Equation (62) in Equation (35) results in the solution of Equation (33)

$$\{X(\bar{\xi})\}=\begin{bmatrix}[\Psi_{11}] & [\Psi_{12}]\\ [\Psi_{21}] & [\Psi_{22}]\end{bmatrix}\begin{bmatrix}[A_{11}(\bar{\xi})] & [A_{12}(\bar{\xi})]\\ [A_{21}(\bar{\xi})] & [A_{22}(\bar{\xi})]\end{bmatrix}\begin{bmatrix}\bar{\xi}^{-[\lambda]} & \\ & \bar{\xi}^{[\lambda]}\end{bmatrix}$$
$$\begin{bmatrix}[\bar{Y}_{11}(\bar{\xi})] & [\bar{Y}_{12}(\bar{\xi})]\\ 0 & [\bar{Y}_{22}(\bar{\xi})]\end{bmatrix}\begin{Bmatrix}\{c_1\}\\ \{c_2\}\end{Bmatrix} \tag{63}$$

For the water sloshing in a tank, the computational domain is a bounded domain ($0\leqslant\xi\leqslant 1$, namely $0\leqslant\bar{\xi}\leqslant\sqrt{2}$). As the real parts of the eigenvalues $[\lambda]$ are negative, if $\bar{\xi}\to 0, \bar{\xi}^{-[\lambda]}\to\infty$, the matrix $[Y_{22}(\bar{\xi})]$ also approaches infinity due to the logarithmic functions in Equation (61). In order to get a finite solution at $\bar{\xi}=0$, the constant $\{c_2\}$ must be zero. Then, Equation (63)

Copyright © 2006 John Wiley & Sons, Ltd.

is written as

$$\{a(\bar{\xi})\} = ([\Psi_{11}][A_{11}(\bar{\xi})] + [\Psi_{12}][A_{21}(\bar{\xi})])\bar{\xi}^{-[\lambda]}[\bar{Y}_{11}(\bar{\xi})]\{c_1\} \tag{64}$$

$$\{q(\bar{\xi})\} = ([\Psi_{21}][A_{11}(\bar{\xi})] + [\Psi_{22}][A_{21}(\bar{\xi})])\bar{\xi}^{-[\lambda]}[\bar{Y}_{11}(\bar{\xi})]\{c_1\} \tag{65}$$

If the moving velocity of the container is known, the $\{q(\bar{\xi})\}|_{\bar{\xi}=\sqrt{2}}$ can be calculated by Equation (22). According to Equation (65), the constant $\{c_1\}$ is calculated by

$$\{c_1\} = (([\Psi_{21}][A_{11}(\bar{\xi})] + [\Psi_{22}][A_{21}(\bar{\xi})])\bar{\xi}^{-[\lambda]}[\bar{Y}_{11}(\bar{\xi})])|^{-1}_{\bar{\xi}=\sqrt{2}}\{q(\bar{\xi})\}|_{\bar{\xi}=\sqrt{2}} \tag{66}$$

By utilizing Equation (12), the velocity of the fluid particle can be directly computed by

$$\{u\} = \nabla\phi = \{b^1(s)\}\{a(\xi)\}_{,\xi} + \frac{1}{\xi}\{b^2(s)\}\{a(\xi)\}_s \tag{67}$$

In Equation (67) the partial derivative of the potential with respect to ξ can be computed by

$$\{a(\xi)\}_{,\xi} = \frac{\partial\bar{\xi}}{\partial\xi}\{a(\bar{\xi})\}_{,\bar{\xi}} = \frac{1}{\bar{\xi}}\{a(\bar{\xi})\}_{,\bar{\xi}} \tag{68}$$

The $\{a(\bar{\xi})\}_{,\bar{\xi}}$ at the nodal points can be calculate according to the differential of Equation (64) with respect to $\bar{\xi}$ directly.

5. NUMERICAL RESULTS

5.1. Water sloshing in containers

The model is firstly applied to simulate the water sloshing in a rectangular water container as shown in Figure 1(a). The water depth in the tank is H, the half-width of the tank is B. The scaled centre is at the centre of the free water surface. Assuming the tank is oscillating in the horizontal direction with an amplitude A and an angular frequency ω. The velocity of the tank motion can be expressed as

$$u = \omega A\cos(\omega t), \quad v = 0 \tag{69}$$

The linear analytic solution of the potential function in the fluid domain is

$$\phi(x,z) = C_0\frac{\sin k_0 x}{\cos k_0 B}Z_0(k_0 z) + \sum_{m=1}^{\infty} C_m\frac{\sinh k_m x}{\cosh k_m B}Z_m(k_m z) \tag{70}$$

where the vertical eigenfunctions $Z_0(k_0 z)$ and $Z_m(k_m z)$ are

$$Z_0(k_0 z) = \cosh k_0(z+H)/\cosh k_0 H$$

$$Z_m(k_m z) = \cos k_m(z+H)/\cos k_m H, \quad m = 1,2,\ldots$$

Copyright © 2006 John Wiley & Sons, Ltd.

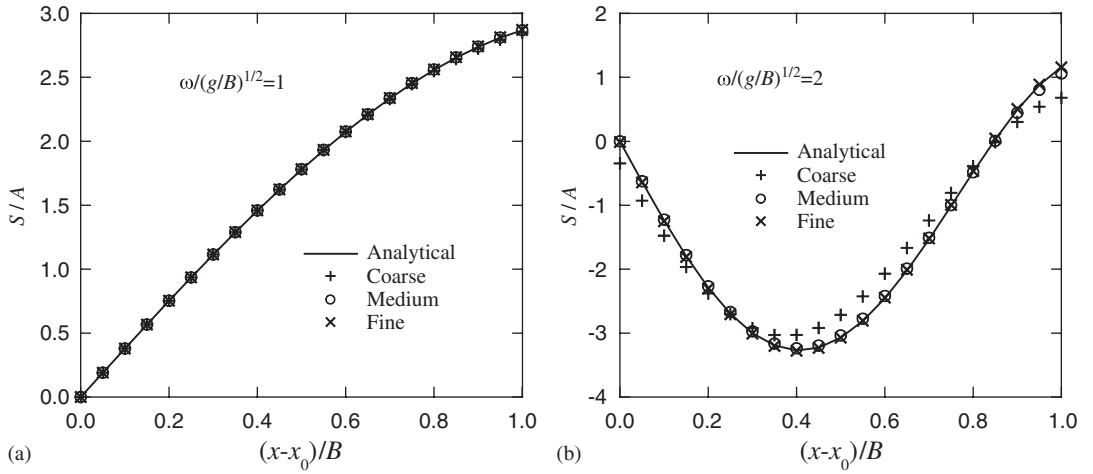

Figure 2. Distribution of the surface elevation at the moment $\omega t = 2n\pi$.

wave number k_0 and k_m are the real roots of the dispersion relations

$$\omega^2 = gk_0 \tanh k_0 H$$

$$\omega^2 = -gk_m \tan k_m H, \quad m = 1, 2, \ldots$$

and the expansion coefficients C_m's are determined by the following equation:

$$C_m = -\frac{\mathrm{i}\omega}{k_m} \int_{-h}^{0} Z_m(k_m z)\,\mathrm{d}z \Big/ \int_{-h}^{0} Z_m^2(k_m z)\,\mathrm{d}z, \quad (m = 0, 1, 2, \ldots)$$

In the SBFEM, only the boundary of the fluid domain is discretized into boundary finite elements. For the computation shown in Figure 1(a), the tank has a relative water depth of $H/B = 1$. The two sidewalls and the bottom of the tank are discretized into several three-node second-order finite elements. In order to investigate the mesh dependence of the method, three different meshes are employed. In the coarse mesh, the bottom boundary is divided into two elements of the same size and each sidewall is divided into one element. The medium mesh has twice the element number of the coarse mesh. And the element number of the fine mesh is four times of that of the coarse one.

Figure 2 shows the comparison of the SBFEM solution of the distribution of the wave surface elevation (S) along the still water surface level with the analytical one in cases of $\omega/(g/B)^{1/2} = 1$ and 2 at the moment $\omega t = 2n\pi$ ($n = 0, 1, 2, \ldots$). The water surface elevation can be computed by the potential function at the surface by $S = (\partial\Phi/\partial t)/g = \mathrm{Re}(\mathrm{i}\omega\phi/g)$. Only the results for $x - x_0 > 0$ are plotted in Figure 2 due to the symmetry of the configuration. From Figure 2(a) it can be seen that even the results from the coarse mesh agree very well with the analytical solution when $\omega/(g/B)^{1/2} = 1$. It is seen from Figures 2 that the surface elevation distribution for $\omega/(g/B)^{1/2} = 1$ is very different from that for $\omega/(g/B)^{1/2} = 2$. There is some discrepancy between the SBFEM solution from the coarse mesh and the analytical one when

Copyright © 2006 John Wiley & Sons, Ltd.

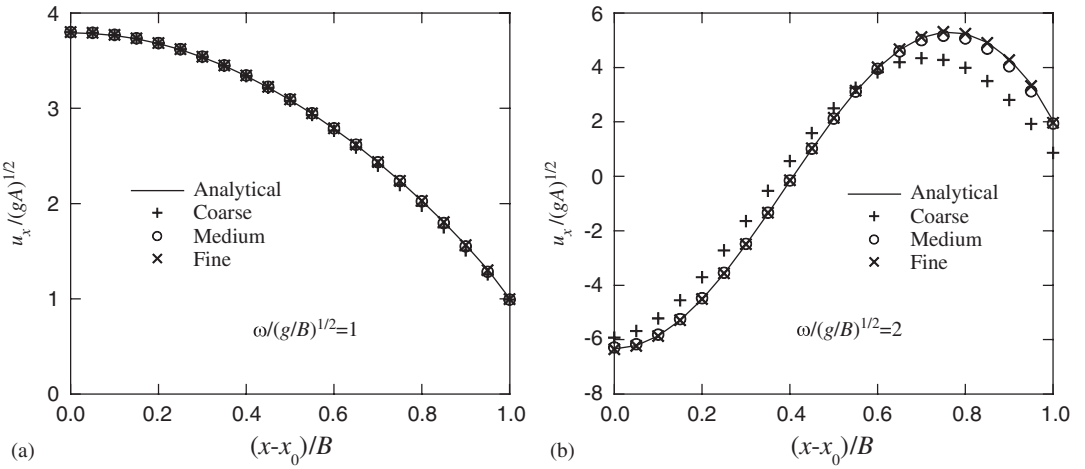

Figure 3. Distribution of the horizontal velocity along water surface at the moment $\omega t = 2n\pi$.

$\omega/(g/B)^{1/2} = 2$. However, the SBFEM solutions from the medium mesh and the fine mesh agree well with the analytical one.

Figure 3 shows the comparison of the distribution of the horizontal velocity along the water surface with the analytical solution. For $\omega/(g/B)^{1/2} = 1$, the horizontal velocity attains its maximum value at the centre of the tank. It decreases with the increase of x and attains its minimum value as $(x - x_0)/B = 1$. All the three meshes give good prediction of the horizontal velocity in the case of $\omega/(g/B)^{1/2} = 1$. It is seen from Figure 3(b) that the SBFEM result from the coarse mesh is not good. However, the SBFEM results from the medium and the fine meshes are very close to the analytical one.

Figure 4 shows the vertical velocity components along the still water surface. It is seen that the predicted vertical velocity near the position $(x - x_0)/B = 1$ is not as good as the horizontal velocity. The deviation of the SBFEM solution from the analytical solution decreases with the increase of the element number. The SBFEM solution is analytical in the scaled coordinate direction as discussed in Section 2. On the free surface $z = 0$, the horizontal direction coincides with the scaled coordinate. The velocity component in the normal direction of the scaled coordinate is actually calculated by the interpolation of the nodal values of the potential function along the curve $S(\xi)$. This is the reason why the predicted horizontal velocity is better than the vertical one. The velocity in the normal direction of the scaled coordinate can be refined by further reducing the mesh size. Because only the boundary of the domain is divided into three-node elements, the reduction of the mesh size would not increase the CPU time very much. From Figures 2–4 it can be seen that the higher frequency of the water tank oscillating is, the finer mesh is needed in order to give a good prediction of the water movement in the tank.

The SBFEM solution is also compared with the solution from the FEM. When using the FEM to solve the problem, the computational domain is discretized into 4×2 eight-node second-order finite elements. The element number along the bed and that along the sidewall are the same as those in the medium mesh of the SBFEM. Figures 5–7 show the comparison

Copyright © 2006 John Wiley & Sons, Ltd.

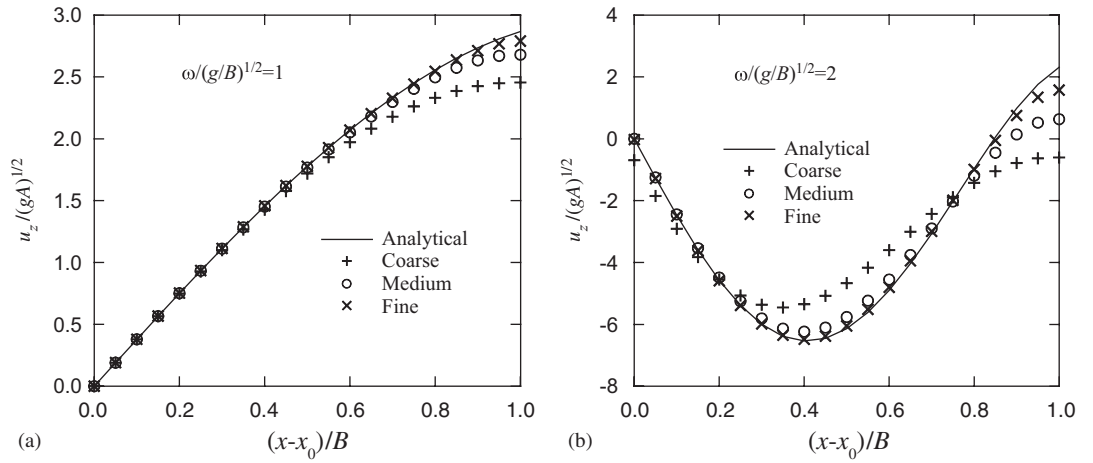

Figure 4. Distribution of the vertical velocity along the water surface at the moment $\omega t = 2n\pi$.

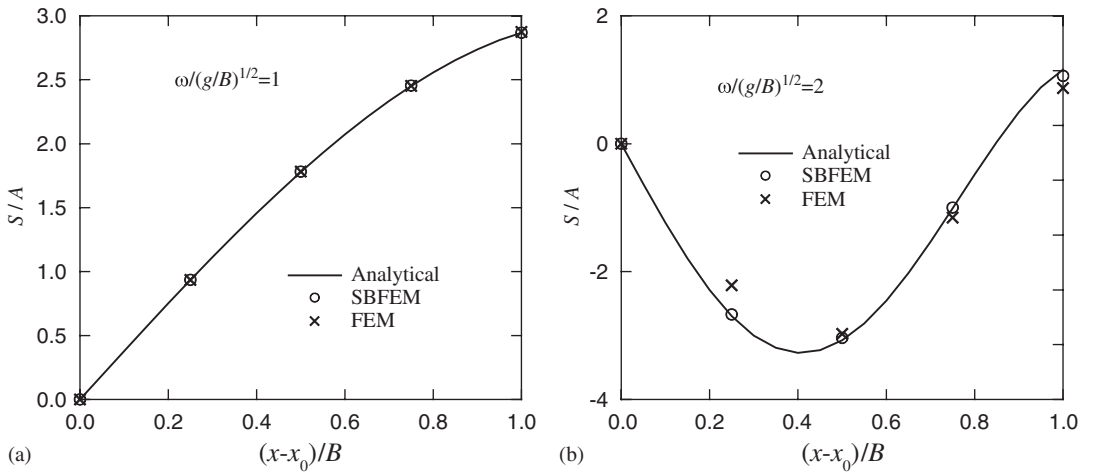

Figure 5. Comparison of the SBFEM and the FEM solutions of surface elevation at the moment $\omega t = 2n\pi$.

of the water surface elevation, the horizontal velocity and the vertical velocity along the water surface, respectively. The SBFEM solutions in Figures 5–7 are from the medium mesh. It can be seen from Figures 5–7 that the SBFEM solution is much better than that of the FEM in the condition of same element size, especially in the high-frequency case. The SBFEM solution is better than the FEM solution is because the analytical procedure is applied in the scaled coordinate direction. The governing equation is actually discretized numerically only in one dimension, which is along the boundary. The FEM method, however, discretize the governing equation in two dimensions. The other advantage of the SBFEM method is that the number

Copyright © 2006 John Wiley & Sons, Ltd.

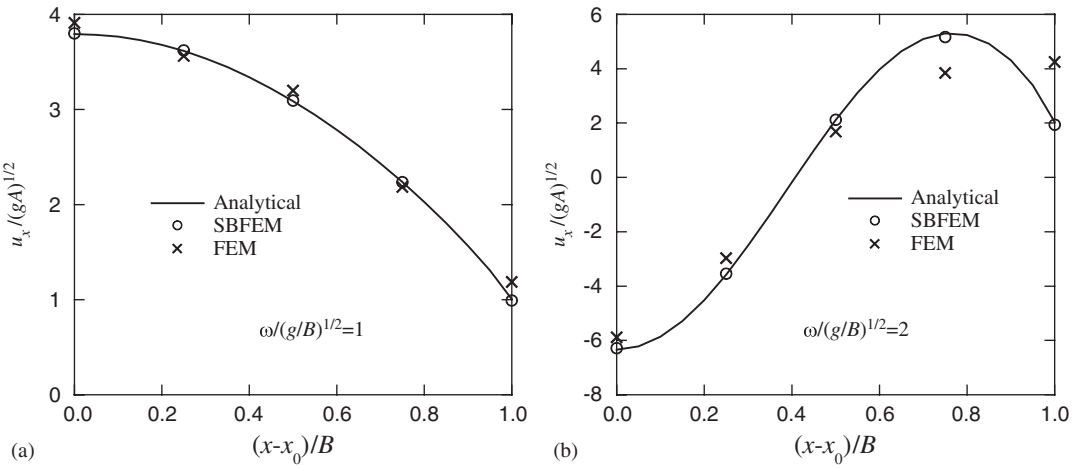

Figure 6. Comparison of the SBFEM and the FEM solutions of the horizontal velocity along the water surface at the moment $\omega t = 2n\pi$.

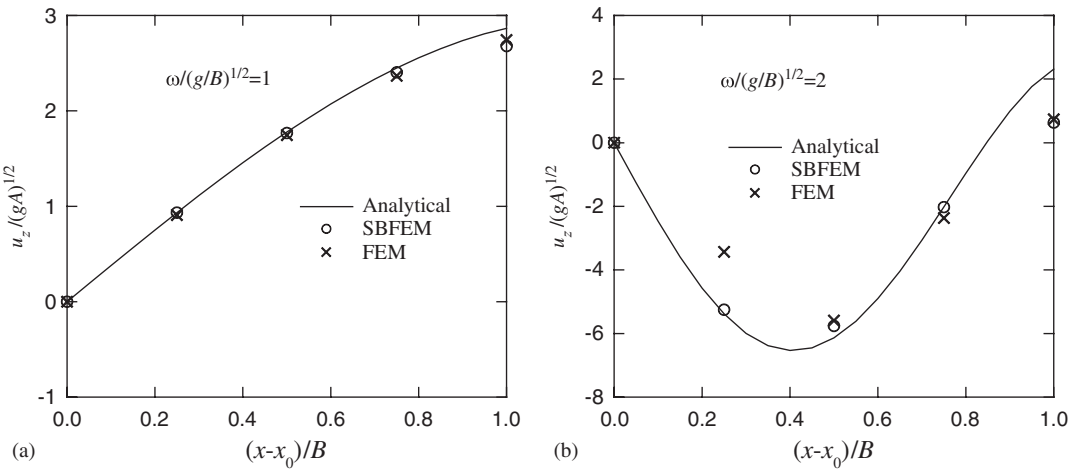

Figure 7. Comparison of the SBFEM and the FEM solutions of the vertical velocity along the water surface.

of the nodal points of meshes is much less than that of the FEM method because only the boundary is discretized.

In order to investigate the effect of the oscillating frequency on the amplitude of the fluctuating water surface, the distributions of the wave amplitude along the x-direction for different values of frequency are plotted in Figures 8. Figure 8(a) is of the case that the tank is oscillating in the horizontal direction and Figure 8(b) is of the case that the tank is rotationally

Copyright © 2006 John Wiley & Sons, Ltd.

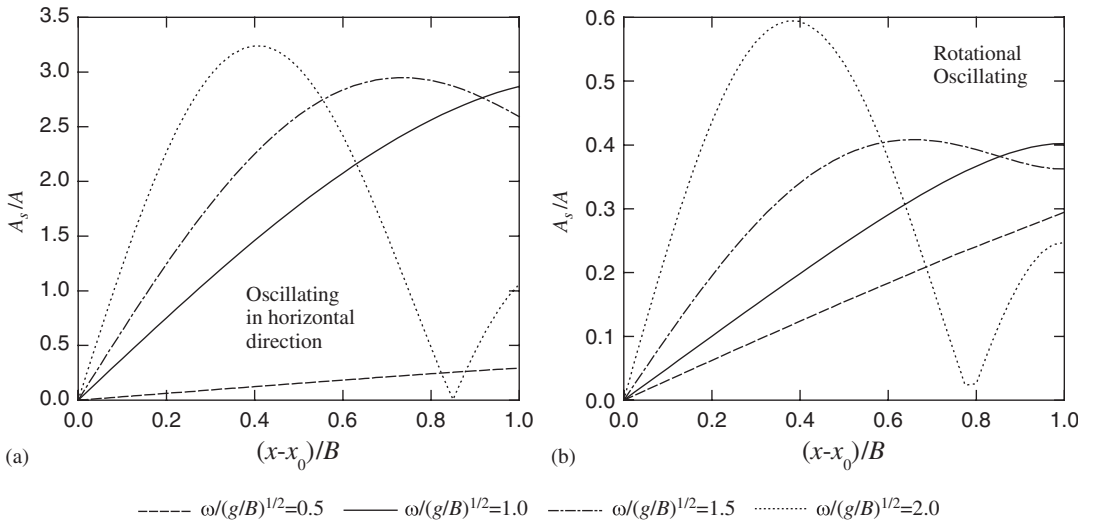

Figure 8. Distribution of the amplitude along x-direction for different values of $\omega/(g/B)^{1/2}$ for a rectangular tank.

oscillating with respect to the centre point of the still water surface. The amplitude A in Figure 8(b) is the vertical oscillating amplitude of the left and right points of the still water surface. It is found that the oscillating frequency affects the wave amplitude distribution very much. When the frequency is small, the maximum amplitude is located at the sidewall of the tank ($(x-x_0)/B=1$). And the amplitude of the water surface approaches to the linear relation with x when frequency is very small. At larger value of frequency, the maximum amplitude of water profile is not at the sidewall but in the inner area of the tank. It is seen from Figures 8(a) and (b) that there is a point around $(x-x_0)/B=0.8$ in which the amplitude is close to zero for $\omega/(g/B)^{1/2}=2$. The amplitude of the water surface when the container is oscillating in the horizontal direction is much larger than that when the container is rotational oscillating.

In the practical engineering, the water surface elevation at the sidewall is the most important factor because the height level should not exceed the wall height. Figure 9 shows the variation of the surface amplitude at the sidewall ($(x-x_0)/B=1$) with the oscillating frequency for a rectangular tank at different values of H/B. Figure 9(a) is the case of tank oscillating in the horizontal direction and Figure 9(b) is the case that the tank is oscillating with respect to the centre point of the still water surface. It is found from Figure 9 that the resonance occurs at resonance frequencies. It is seen that the resonance frequencies in Figure 9(a) are identical to those in Figure 9(b). For a rectangular tank oscillating in the horizontal direction, the resonance frequencies ω_r can be computed analytically by

$$\frac{\omega_r^2}{gB}=(n+0.5)\pi\tanh((n+0.5)\pi H/B),\quad n=1,2,3,\ldots \tag{71}$$

The computed resonance frequencies are compared with the analytical ones in Table I. It is found that the numerical results of the resonance frequencies are almost identical to the

Copyright © 2006 John Wiley & Sons, Ltd.

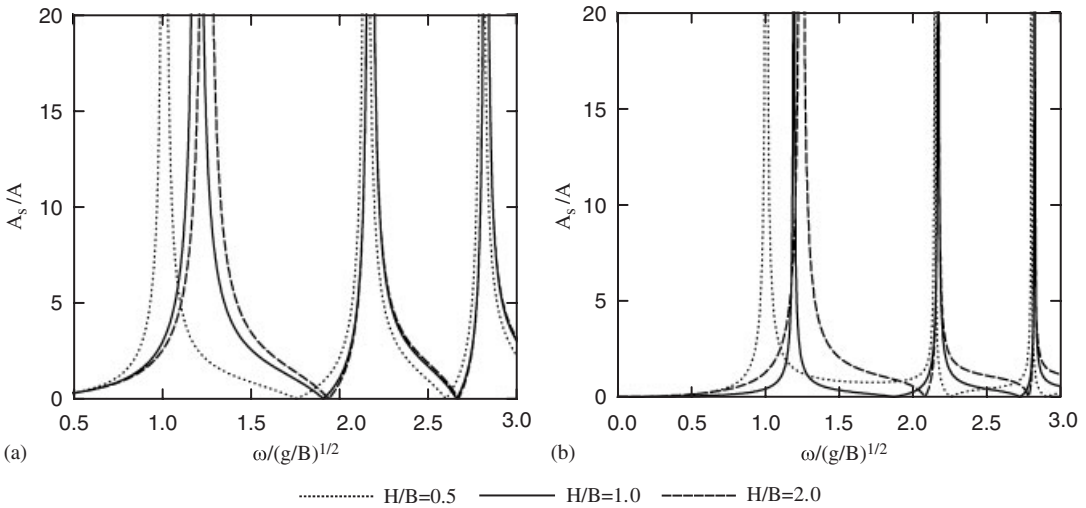

Figure 9. Variation of the amplitude at the sidewall with frequency for a rectangular tank: (a) oscillating in horizontal direction; and (b) rotational oscillating with respect to centre point of still surface.

Table I. Comparison of the resonance frequencies for rectangular tank oscillating in the horizontal direction.

n	$n=0$			$n=1$			$n=2$		
H/B	0.5	1.0	2.0	0.5	1.0	2.0	0.5	1.0	2.0
Analytical	1.015	1.200	1.250	2.151	2.170	2.170	2.801	2.802	2.802
Numerical	1.015	1.200	1.250	2.157	2.175	2.175	2.805	2.824	2.825

analytical ones. From Equation (71) it can be seen that for the first few models the dimensionless resonance frequencies is relative to the tank depth. When n is large, the dimensionless resonance frequencies of different tanks are the same. The increase of the square of the dimensionless resonance frequency is π. Thus, with the increases of frequency the interval between two successive resonance frequencies decreases.

Figure 10 is the variation of the amplitude at the sidewall with the frequency for a hemicircular tank as shown in Figure 1(b). It is seen that the variation of the wave amplitude with the frequency is similar with that of the rectangular tank.

5.2. Water sloshing in a tank with an obstacle on the bed

The water sloshing in a tank with a square obstacle located in the centre of the bed (as shown in Figure 11) is simulated. The boundary length of the square obstacle is 0.4 times of the half-width B of the tank. The still water depth in the tank is B. In order to use the SBFEM to simulate the water sloshing, the flow field is divided into three sub-domains as shown in Figure 12. Computations are carried out for $\omega/(g/B)^{1/2}=2$. Three meshes of different densities

Copyright © 2006 John Wiley & Sons, Ltd.

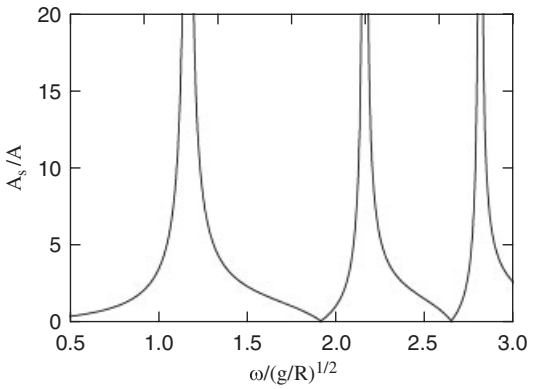

Figure 10. Variation of the amplitude at the sidewall with frequency for a hemi-circular tank.

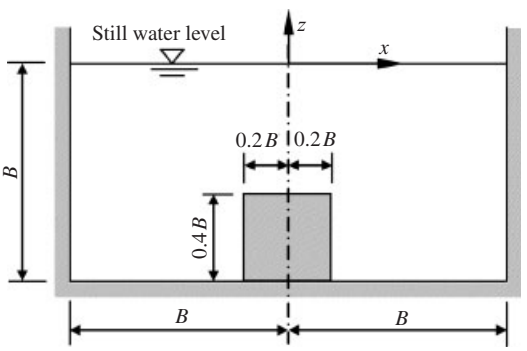

Figure 11. Configuration of the water sloshing in a rectangular tank with a square obstacle.

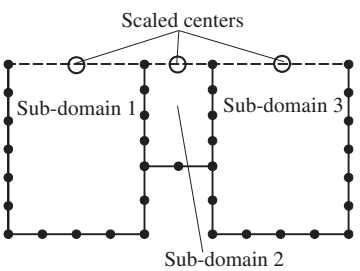

Figure 12. Element distribution of the coarse mesh.

are applied in order to investigate the mesh dependent of the method. Figure 12 shows the element distribution of the coarse mesh. In Section 5.1 we found that the medium mesh can give a good prediction of the vertical velocity for $\omega/(g/B)^{1/2} = 2$, whereas the coarse mesh cannot. In this example, the density of the coarse mesh is similar to that of the medium mesh

Copyright © 2006 John Wiley & Sons, Ltd.

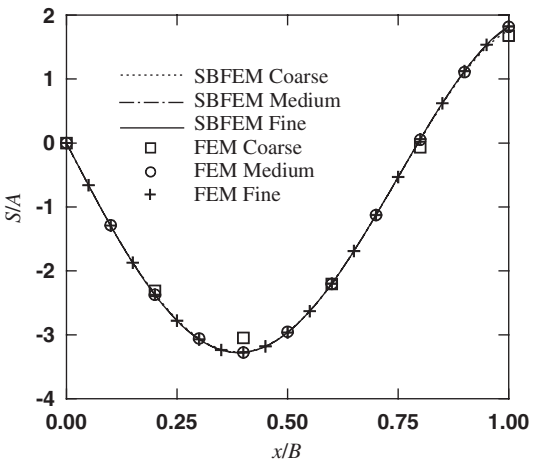

Figure 13. Water surface elevation at the moment $\omega t = 2n\pi(\omega/(g/B)^{1/2} = 2)$.

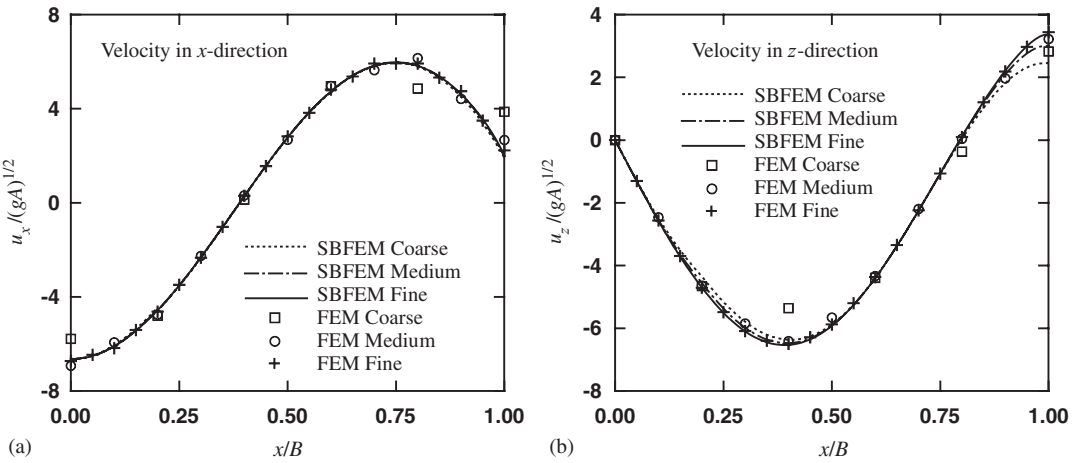

Figure 14. Velocity distribution along the water surface at the moment $\omega t = 2n\pi(\omega/(g/B)^{1/2} = 2)$.

used in Section 5.1. The mesh density of the medium mesh and that of the fine mesh are two times and four times of the coarse mesh's density shown in Figure 12, respectively. Figure 13 shows the computed water surface elevation from these three meshes. The FEM solutions are also plotted in Figure 13 for comparison. The sizes of the coarse, medium and fine meshes of the FEM method are equal to their counterpart of the SBFEM method. It can be seen that the SBFEM solutions from the three meshes are almost identical. The FEM solution from the fine mesh is very close to the SBFEM solution. There are some discrepancies among the FEM solutions from the coarse, medium and fine meshes. Figure 14 shows the comparison of the SBFEM solution of the velocity at the water surface with the FEM solution. It can be seen that for the velocity in the x-direction there is little difference among the three sets of SBFEM

Copyright © 2006 John Wiley & Sons, Ltd.

solutions. However, the difference among the three sets of FEM solutions are obviously. For the velocity in the z-direction, there is little difference among the SBFEM solutions from the three meshes when x/B is less than 0.8. When x/B approaches 1.0, there are some differences among the three SBFEM results. FEM results from the three meshes diverge not only when x/B approaches 1.0, but also at about $x/B = 0.4$. From the above comparison we can see that good results can be got even from coarse mesh by using the SBFEM method.

6. CONCLUSIONS

A scaled boundary finite element numerical model (SBFEM) is developed for simulating the water sloshing in a rectangular water container. In the numerical model, only the boundary of the computational domain is discretized using the SBFEM. The SBFEM reduced the 2D problem to a 1D one. The SBFEM results of the water surface elevation and the velocity are compared with the analytical solution and the FEM solution. Because the analytical method is applied in the scaled coordinate direction, it is shown that the predicted SBFEM solution of the velocity component in the direction of the scaled coordinate is very close to the analytical one, and is much better than the FEM solution in case of same mesh size. Whereas the velocity components in the normal direction of the scaled coordinate is not as good as that in the scaled coordinate direction. However, the velocity in this direction is still much better than the FEM solution. The resonance of the water tank is also predicted by the SBFEM model and the resonance frequencies agree very well with the analytical ones. The present model can also applied to the cases that the shape of the water container is not rectangular in which the analytical solution is unavailable. The model can be employed to complex domains by using multiple sub-domains. This method is applied to simulate the water sloshing in a rectangular tank with a square obstacle on the bed. The numerical results demonstrate that the sub-domain method can also give better results than the FEM method.

ACKNOWLEDGEMENTS

This research was supported by the National Natural Science Foundation of China, Grant No. 10372020, and a Program for Changjiang Scholars and Innovative Research Team in University, Grant No. IRTO420.

REFERENCES

1. Wolf JP, Song Ch. *Finite-element Modelling of Unbounded Media*. Wiley: Chichester, 1996.
2. Wolf JP, Song C. The scaled boundary finite-element method—a primer: derivations. *Computers and Structures* 2000; **78**:191–210.
3. Song C, Wolf JP. Consistent infinitesimal finite-element cell method: three-dimensional vector wave equation. *International Journal for Numerical Methods in Engineering* 1996; **39**:2189–2208.
4. Deeks AJ, Cheng L. Potential flow around obstacles using the scaled boundary finite-element method. *International Journal for Numerical Methods in Fluids* 2003; **41**:721–741.
5. Li B, Cheng L, Deeks AJ. Scaled boundary finite-element analysis of wave diffraction by a vertical cylinder. *Civil Engineering Research Report C1843*, The University of Western Australia, 2004.
6. Song C, Wolf JP. The scaled boundary finite-element method: analytical solution in frequency domain. *Computer Methods in Applied Mechanics and Engineering* 1998; **164**:249–264.
7. Song C, Wolf JP. The scaled boundary finite-element method—alias consistent infinitesimal finite-element cell method—for elastodynamics. *Computer Methods in Applied Mechanics and Engineering* 1997; **147**:329–355.

Copyright © 2006 John Wiley & Sons, Ltd.